



Cite this: *J. Mater. Chem. A*, 2018, **6**, 9498

## The electronic structure and band interface of cesium bismuth iodide on a titania heterostructure using hard X-ray spectroscopy†

Dibya Phuyal, <sup>a</sup> Sagar M. Jain, <sup>bc</sup> Bertrand Philippe, <sup>a</sup> Malin B. Johansson, <sup>b</sup> Meysam Pazoki, <sup>d</sup> Jolla Kullgren, <sup>d</sup> Kristina O. Kvashnina, <sup>ef</sup> Matthias Klintenberg, <sup>g</sup> Erik M. J. Johansson, <sup>b</sup> Sergei M. Butorin, <sup>a</sup> Olof Karis<sup>a</sup> and Håkan Rensmo<sup>\*a</sup>

Bismuth halide compounds as a non-toxic alternative are increasingly investigated because of their potential in optoelectronic devices and their rich structural chemistry. Hard X-ray spectroscopy was applied to the ternary bismuth halide  $\text{Cs}_3\text{Bi}_2\text{I}_9$  and its related precursors  $\text{BiI}_3$  and  $\text{CsI}$  to understand its electronic structure at an atomic level. We specifically investigated the core levels and valence band using X-ray photoemission spectroscopy (PES), high-resolution X-ray absorption (HERFD-XAS), and resonant inelastic X-ray scattering (RIXS) to get insight into the chemistry and the band edge properties of the two bismuth compounds. Using these element specific X-ray techniques, our experimental electronic structures show that the primary differences between the two bismuth samples are the position of the iodine states in the valence and conduction bands and the degree of hybridization with bismuth lone pair ( $6s^2$ ) states. The crystal structure of the two layered quasi-perovskite compounds plays a minor role in modifying the overall electronic structure, with variations in bismuth lone pair states and iodine band edge states. Density Functional Theory (DFT) calculations are used to compare with experimental data. The results demonstrate the effectiveness of hard X-ray spectroscopies to identify element specific bulk electronic structures and their use in optoelectronic devices.

Received 29th January 2018  
 Accepted 6th April 2018

DOI: 10.1039/c8ta00947c  
[rsc.li/materials-a](http://rsc.li/materials-a)

## 1 Introduction

Mixed organic–inorganic lead halide perovskite optoelectronic devices have shown remarkable progress and development within a short period of time.<sup>1,2</sup> Their record-breaking efficiency and application in various technologies have generated a substantial effort towards exploring new perovskite-like compounds.<sup>3–8</sup> The flexibility of substitution of cation and

anion elements, as well as compositional doping, allows for improved functionality, new characteristics, and a rich phase diagram. One of the key attributes of perovskites lies in the processing of thin films through various solution processes<sup>9,10</sup> or evaporation<sup>11–13</sup> to achieve high-yield crystalline thin films, enabling a realistic pathway for large-scale fabrication and ease of application.

The lead halide constituent (e.g.,  $\text{MAPbI}_3$  and its analogues) of new solar materials has garnered the most attention; however toxicity<sup>14</sup> and stability remain a challenge to address.<sup>15,16</sup> Inorganic perovskite materials display a better stability towards moisture, light soaking, and thermal stressing which ensures their long-term stability in solar cells and related optoelectronic devices. Additionally, the high band gap offered by these inorganic perovskites makes their use in tandem solar cells viable. Therefore, exploring inorganic alternative heavy elements with variable cation and anion substitutions, such as bismuth-based halides, potentially offers a new route to unique material properties. The ternary bismuth halide  $\text{Cs}_3\text{Bi}_2\text{I}_9$  has been investigated by several groups because of its application in solar cells and optoelectronics with encouraging results.<sup>17–19</sup> The related  $\text{BiI}_3$  has also been effective in its use for various optoelectronic applications itself,<sup>20–22</sup> while  $\text{CsI}$  has been used for high-energy detectors for decades.<sup>23</sup> In alternative metal cation substitutions, the oxidation sensitive tin iodides<sup>24</sup> or the

<sup>a</sup>Division of Molecular & Condensed Matter, Department of Physics, Uppsala University, Box 516, SE-75121, Uppsala, Sweden. E-mail: [hakan.rensmo@physics.uu.se](mailto:hakan.rensmo@physics.uu.se); Tel: +46 18 471 3547

<sup>b</sup>Division of Physical Chemistry, Department of Chemistry, Uppsala University, Box 516, SE-75121, Uppsala, Sweden Stockholm, Sweden

<sup>c</sup>SPECIFIC, College of Engineering, Swansea University Bay Campus, Fabian Way, SA1 8EN Swansea, UK

<sup>d</sup>Department of Chemistry, Structural Chemistry, Ångström Laboratory, Uppsala University, Box 538, 752 21, Uppsala, Sweden

<sup>e</sup>Rossendorf Beamline at ESRF – The European Synchrotron, CS40220, 38043 Grenoble Cedex 9, France

<sup>f</sup>Helmholtz Zentrum Dresden-Rossendorf (HZDR), Institute of Resource Ecology, PO Box 510119, 01314 Dresden, Germany

<sup>g</sup>Division of Materials Theory, Department of Physics, Uppsala University, Box 516, SE 75121, Uppsala, Sweden

† Electronic supplementary information (ESI) available: A table for the selected distances in the crystal structure of  $\text{Cs}_3\text{Bi}_2\text{I}_9$  and  $\text{BiI}_3$ , HAXPES Bi 4f core level spectra, and UV-Vis experimental Tauc plots (PDF). See DOI: 10.1039/c8ta00947c



moisture sensitive  $\text{Sb}^{3+}$  iodides are serious concerns, nevertheless they have merits of their own in their crystal and electronic properties.

The chemical properties of bismuth and lead based perovskites adopt the stable  $\text{d}^{10}\text{s}^2\text{p}^0$  electronic configuration. The lone pair electrons ( $6s^2$ ) around the Bi cation form bonding and anti-bonding states in the frontier electronic structures.<sup>25</sup> This specific electronic configuration leads to an increased overlap that results in a larger bandwidth of the valence band.<sup>26</sup> This in turn will result in intrinsic point defects giving rise to shallow defect states within the valence band. Additionally, a dependence of the effective charge on the Bi atom and a high dielectric constant<sup>27</sup> have been shown to be beneficial for photovoltaic applications.<sup>28</sup> The facile material processing of these materials further promises their use in large area deposition. However, research into their experimental electronic structure is limited, as well as their interfacial properties. Therefore, in this direction we present a systematic study on  $\text{Cs}_3\text{Bi}_2\text{I}_9$  to provide insights into its electronic structure as well as its energy matching relevant for optoelectronic function/application.

The crystal structure and related phase transitions have been extensively studied through neutron diffraction studies.<sup>29,30</sup> The indirect optical band gap has been estimated to be  $E_g = 2.2$  eV from UV-Vis studies ( $\text{BiI}_3$ : 1.67 eV,  $\text{CsI}$ : 6.2 eV).<sup>31</sup> This gap corresponds to covalent Bi 6p/6s and I 5p characters at the top of the valence band (VB) and mostly Bi 6p at the bottom of the conduction band (CB).<sup>18</sup> The large size and radius of the ionic cation (Cs) have largely been argued to play a minor role in the frontier electronic structure. The room temperature crystal structure of  $\text{Cs}_3\text{Bi}_2\text{I}_9$  is a layered perovskite that consists of metal halide octahedral layers and voids in-between are filled by  $\text{Cs}^+$  cations. The metal halide octahedra can be joined at edges or vertices.  $\text{Cs}_3\text{Bi}_2\text{I}_9$  is a face-sharing bi-octahedral ( $\text{Bi}_2\text{I}_9$ )<sup>-</sup> and the 2D layered  $\text{BiI}_3$  is edge-sharing as shown in Fig. 1.

We use synchrotron-based X-ray spectroscopy methods to probe the electronic structure. The sensitivity to local coordination and associated hybridization can provide links between the structure and observed optical properties. The element-specific probe can show differences in the electronic structure

induced by structural changes beyond the directly coordinating atoms. The interfacial energetics from photoemission spectroscopy and band structure calculations are used to interpret an energetically favorable transport at the  $\text{TiO}_2/\text{Cs}_3\text{Bi}_2\text{I}_9$  interface. In order to study this directly, we use for the first time on bismuth halides the combination of hard X-ray photoelectron spectroscopy (HAXPES), partial fluorescence X-ray absorption spectroscopy (XAS, partial fluorescence yield mode), and resonant inelastic X-ray spectroscopy (RIXS). However, there are reports using HERFD-XAS and HAXPES on lead-based perovskite halides.<sup>32,33</sup> By means of complementary X-ray spectroscopy techniques, the obtained data can be used to gain a detailed understanding of the electronic structure of our bismuth-halide based materials. The data are compared against density functional theory (DFT) calculations to reveal information on photovoltaic optical transitions and device design strategies.

## 2 Experimental

### 2.1 Thin film synthesis

Thin films of  $\text{CsI}$ ,  $\text{BiI}_3$ , and  $\text{Cs}_3\text{Bi}_2\text{I}_9$  were synthesized by a solution-based process through mixtures of appropriate precursor ratios. In short,  $\text{CsI}$  and  $\text{BiI}_3$  were dissolved in anhydrous *N,N'*-dimethylformamide (DMF) and dimethyl sulfoxide solution (7 : 3) in a 3 : 2 molar ratio. The solution mixture was boiled at 100 °C for 3 hours inside a  $\text{N}_2$  fluxed dry box. Mesoscopic  $\text{TiO}_2$  (m $\text{TiO}_2$ ) films were deposited on conducting FTO (fluorine-doped tin oxide) glass by spin coating at 3000 rpm for 30 s. The  $\text{TiO}_2$  paste was prepared by diluting Dyesol paste (30NR-T, particle size  $\approx$  30 nm) with ethanol in a 1 : 4 weight ratio. The m $\text{TiO}_2$ -coated glass was annealed on a hot plate at 100 °C for 30 min. The film thickness was  $\approx$  350 ( $\pm$ 50 nm) as determined using a Dektak3 profiler. The bismuth halide perovskite precursor solutions were coated onto the  $\text{TiO}_2$ /FTO substrate by spin-coating at 3500 rpm for 30 s, followed by annealing on a hot plate at 140 °C for 30 min in a dry air box (relative humidity less than 30%).

### 2.2 Hard X-ray photoemission spectroscopy (HAXPES)

HAXPES was carried out at BESSY II (Helmholtz Zentrum Berlin) at the KMC-1 beamline using the HIKE end-station.<sup>34</sup> A photon energy of 4000 eV is selected using first-order light from a Si (311) double-crystal monochromator (Oxford-Danfysik). Photoelectron spectra were recorded using a Scienta R4000 analyzer, optimized for high kinetic energies. At 4000 eV photon energy, a probing depth slightly below 20 nm is expected for the core levels reported here. The incident angle between the beam and the surface of the sample was  $\sim$ 5°, while the photoelectrons were detected close to normal emission,  $\sim$ 85°. The pressure in the analysis chamber was  $\sim$ 10<sup>-8</sup> mbar. The spectra presented were energy calibrated relative to the Au 4f<sub>7/2</sub> core level binding energy which we set to 84.0 eV. The spectra were intensity calibrated using the most intense peak, if not stated otherwise. Intensity ratios presented between different core levels were calculated from the experimental results after correcting for photoionization cross-sections using database values.<sup>35</sup>

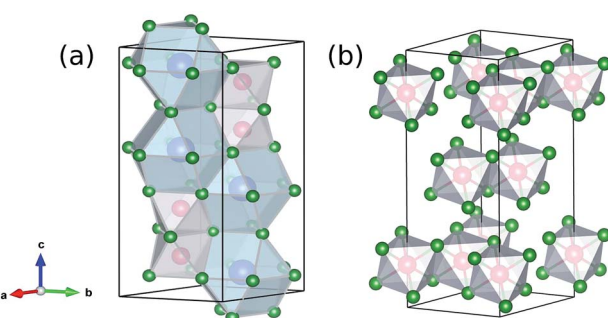


Fig. 1 Schematic crystal structure of  $\text{Cs}_3\text{Bi}_2\text{I}_9$  (a) and  $\text{BiI}_3$  (b) that show layered octahedra that form a distorted cell. Vacancies are characteristic of this crystal structure. Bismuth atoms are shown in red, iodine in green, and cesium in blue.



### 2.3 HERFD-XANES & RIXS

The High Energy Resolution Fluorescence Detected X-ray Absorption Near Edge Structure (HERFD-XANES) and Resonant Inelastic X-ray Scattering (RIXS) spectroscopy experiments were performed at the European Synchrotron Radiation Facility (ESRF).<sup>36,37</sup> The HERFD-XANES (henceforth referred to as simply HERFD) spectra have been described previously.<sup>38</sup> Bismuth L<sub>1</sub> and L<sub>3</sub> HERFD spectra were collected at the BM20 (ROBL) beamline using Si (880) and Ge (884) analyzers respectively. The HERFD-XANES spectra were recorded at the maximum of L<sub>63</sub> and L<sub>o1</sub> emission lines for Bi L<sub>1</sub> and L<sub>3</sub> absorption edges respectively. The overall resolution of HERFD data at the bismuth L<sub>1</sub> and L<sub>3</sub> edges is approximately 4.3 eV and 2.4 eV (including core-hole lifetime broadening) respectively. HERFD measurements at the iodine L<sub>1</sub> edge were performed at the beamline ID26. Spectra were recorded at the maximum of the L<sub>γ2,3</sub> emission line ( $E = 5065$  eV) with a resolution of 2.2 eV. RIXS spectra were recorded near the iodine L<sub>1</sub> edge in the energy range of 5173–5196 eV with a resolution of 0.7 eV as determined from the full width at half maximum (FWHM) of the elastic peak. The energy in HERFD and RIXS was selected using the (331) reflection of three spherically bent Si crystal analyzers. The intensity was normalized to the incident flux measured using a photodiode. The spectrometer energy was calibrated using the elastic peak. Samples were positioned at 45° to the beam. A helium-filled bag was used to reduce absorption effects between the sample and crystal analyzer. Measurements were carried out on multiple spots on the samples to assess radiation damage. The spectra showed no detectable change within the acquisition time (5 min for HERFD and 25 min for RIXS).

### 2.4 Computational

The calculations were carried out using an all electron full-potential linear muffin-tin orbital (FP-LMTO) method<sup>39</sup> within the local density approximation (LDA) with spin-orbit coupling. The full-potential indicates that there are no geometrical

constraints on the expansion of the density and potential (*c.f.* atomic sphere approximation (ASA) where spheres are used). Details on the implementation of the present FP-LMTO method can be found in ref. 39. It should be mentioned that we use an extended basis to eliminate or at least significantly reduce the solution dependence of the tail energies in the basis set, in the calculations. The FP-LMTO method used here is an all electron implementation meaning that no pseudo-potentials are used. The core electrons are treated explicitly by solving the Dirac equation and this process is part of the self-consistent loop, *i.e.* the core-density is relaxed at each iteration. Technical parameters such as the  $k$ -point grid and fast Fourier transform (FFT) mesh were set to give a converged electronic structure. In the present calculations the muffin-tin radii are maximized iteratively to cover 90% of the nearest neighbor distance. The input structures were taken from the literature on Cs<sub>3</sub>Bi<sub>2</sub>I<sub>9</sub> (ref. 40) and BiI<sub>3</sub>.<sup>41</sup> The calculated results are part of the electronic structure project, where the computational methods are also described in more detail.<sup>42</sup>

## 3 Results and discussion

### 3.1 Photoelectron spectroscopy

Fig. 2 shows overview spectra of a TiO<sub>2</sub>/Cs<sub>3</sub>Bi<sub>2</sub>I<sub>9</sub> sample along with the precursors BiI<sub>3</sub> and CsI to qualitatively follow the characteristic change in the electronic structure. All samples show their distinct core peaks, including some substrate peak contributions (Ti 2p and O 1s). Carbon and nitrogen peaks are negligible in intensity, indicating a minor contribution from surface contamination. Core-level intensity variations and the effect on the electronic signature will be discussed later.

Core level spectra for Bi 4f, I 3d, and Cs 3d are presented in Fig. 3. The main contributions for Cs<sub>3</sub>Bi<sub>2</sub>I<sub>9</sub> and BiI<sub>3</sub> 4f<sub>7/2</sub> have peak maxima at 159.5 eV and 158.9 eV respectively (BiI<sub>3</sub> Fig. S1†) a difference of 0.5 eV. Cs 4p (grey fill) and Bi 4f (blue fill) have an overlap near 161 eV. There is a small peak at lower binding energy from the main 4f<sub>7/2</sub>, indicating a metallic Bi ( $\approx 157.0$  eV, brown fill) component present in both samples, likely an

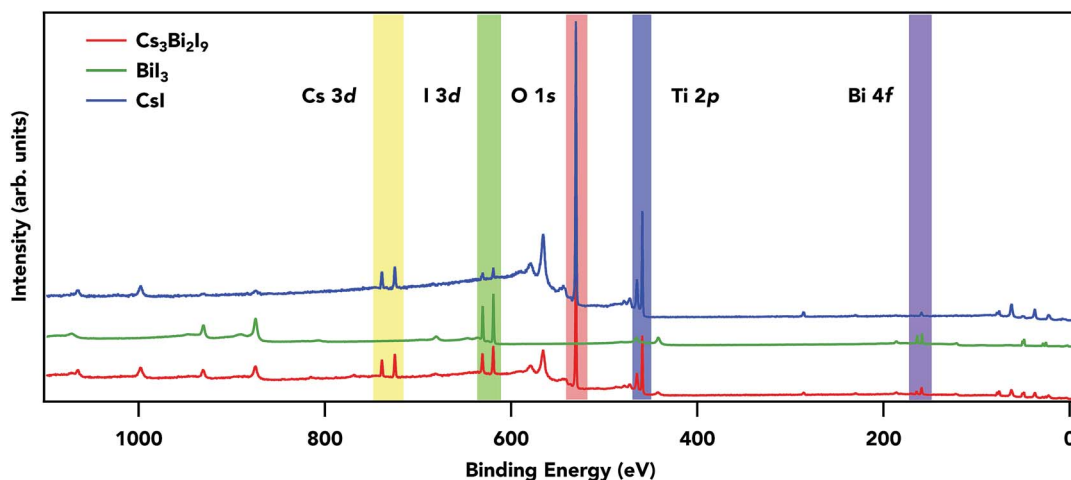


Fig. 2 Survey spectra for precursor materials and the quasi-perovskite Cs<sub>3</sub>Bi<sub>2</sub>I<sub>9</sub> measured at 4000 eV. The spectra are normalized to I 3d peaks.



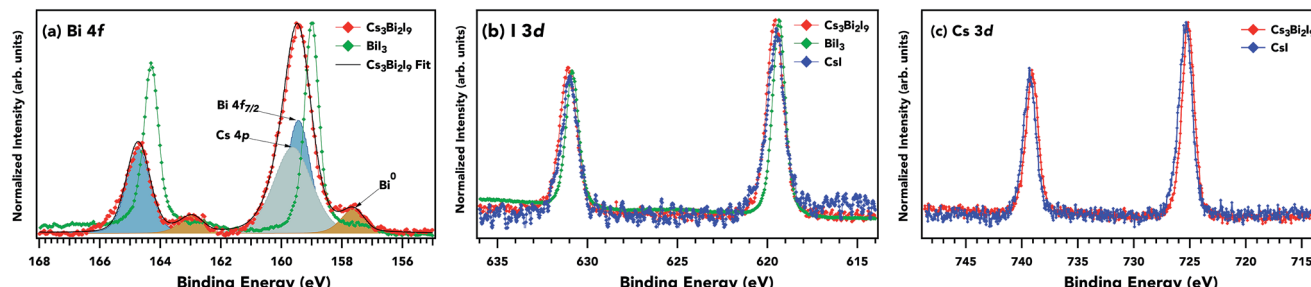


Fig. 3 (a) Core level peaks for bismuth 4f for  $\text{Cs}_3\text{Bi}_2\text{I}_9$  and  $\text{BiI}_3$ . The Bi 4f spectrum for  $\text{Cs}_3\text{Bi}_2\text{I}_9$  experimental (red markers) and fitted spectra (black line) overlap with  $\text{Cs} 4p$  (grey fill) at around  $\approx 161$  eV.  $\text{BiI}_3$  peak, shown with green markers, shows a small shift towards lower binding energy and a narrower width than  $\text{Cs}_3\text{Bi}_2\text{I}_9$ . The spectra are normalized to Bi 4f<sub>7/2</sub> peak intensity. The gold fill shows the Bi metallic component. (b) I 3d spectra (right) show a narrower width for  $\text{BiI}_3$  with little modification in binding energy positions. (c) Cs 3d core level spectra.

outcome of improper crystallization of thin films during synthesis. Metallic components in halide perovskites have been strongly linked to iodine deficiencies and vacancies,<sup>43</sup> dissociation of precursor species during synthesis,<sup>44</sup> and annealing processes.<sup>45,46</sup> The primary bismuth peak shifted nearly 2 eV from the metallic, which is characteristic of  $\text{Bi}^{3+}$  oxidation, as reported in work by Park *et al.*<sup>17</sup> The core-level Bi 4f<sub>7/2</sub> maxima for  $\text{Cs}_3\text{Bi}_2\text{I}_9$  and  $\text{BiI}_3$  differ by 0.54 eV. The FWHM difference can be attributed to disorder in the  $\text{Cs}_3\text{Bi}_2\text{I}_9$  sample since all other contributions to the Bi 4f linewidth should be the same. Slight differences in the environment of the Bi from site to site (*e.g.* as vacancies, substitutional disorder, and structural variations) result in small changes in the binding energy position which contribute to an overall core-level broadening. The small modifications in the core level width and position can be rationalized in terms of a higher charge density around the Bi atom for the face-sharing octahedra for  $\text{Cs}_3\text{Bi}_2\text{I}_9$  compared to the edge-sharing octahedra for  $\text{BiI}_3$ . The I 3d core level peak is at a binding energy of 619.5 eV, 619.4 eV, and 619.5 eV for the  $\text{Cs}_3\text{Bi}_2\text{I}_9$ ,  $\text{BiI}_3$ , and  $\text{CsI}$  samples respectively. The spin-orbit splitting is 11.5 eV in the I 3d<sub>3/2</sub> level for all samples, and the binding energy positions, indicating a monovalent iodine atom in each of the samples with a similar coordination.

An approximate estimation of the material stoichiometry can be made using the relative intensities of the experimental core levels. In such a calculation one needs to take into account the differential cross-sections and angle between the photoelectrons and the polarization direction of the X-rays.<sup>47,48</sup> The stoichiometry estimation for I/Bi in  $\text{Cs}_3\text{Bi}_2\text{I}_9$  is 4.34, reasonably close to the expected value of 4.5 when using Bi 5d and I 4d core levels. The cesium to iodide is 2.7 using Cs 4d and I 4d, also expected for  $\text{Cs}_3\text{Bi}_2\text{I}_9$ . The experimental stoichiometry for  $\text{BiI}_3$  is 2.9, close to the expected value of 3, and finally 0.98 for  $\text{CsI}$  as expected. The matching between the experimental values and expected values from the stoichiometry supports the high quality of the samples. For these materials, effects from surface segregation or reconstruction are limited due to the bulk probe of the high photon energies.

### 3.2 X-ray absorption & emission spectroscopy

The HERFD-XANES helps to reduce the core-hole broadening of XANES spectra by monitoring the specific emission line as

scanning across an absorption edge.<sup>49</sup> This second-order process mitigates the inherent core-hole lifetime broadening. Fig. 4 shows the normalized (normalized at the higher energy side of the spectrum) Bi L<sub>1</sub> (Fig. 4a) and L<sub>3</sub> (Fig. 4b) absorption edges of  $\text{Cs}_3\text{Bi}_2\text{I}_9$  along with  $\text{BiI}_3$ . The edge positions for the Bi L<sub>1</sub> edges for the two samples studied are practically equivalent ( $\text{Cs}_3\text{Bi}_2\text{I}_9$  L<sub>1</sub>: 16 388.5 eV,  $\text{BiI}_3$  L<sub>1</sub>: 16 388.9 eV, determined by the maximum of the second derivative), as expected for samples with the same formal Bi valence state ( $\text{Bi}^{3+}$ ). The strong peak near  $\sim 16\ 395$  eV is a so-called 'white line' feature and is ascribed to transitions from  $2s \rightarrow 6p$  states, just above the Fermi energy ( $E_F$ ). High-energy structures, *i.e.* features a few eV

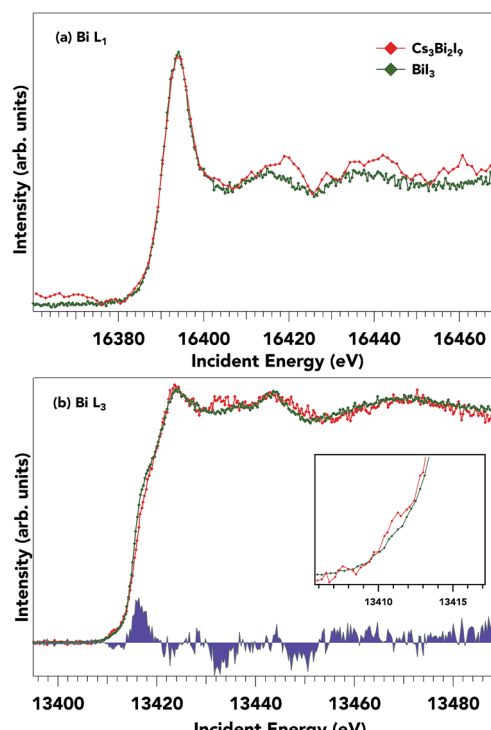


Fig. 4 (a) Bismuth L<sub>1</sub> and (b) bismuth L<sub>3</sub> HERFD-XANES spectrum for  $\text{Cs}_3\text{Bi}_2\text{I}_9$  and  $\text{BiI}_3$ . Although the Bi L<sub>1</sub> edge has a low signal-to-noise ratio, the spectrum can still be used to describe the chemical state. The L<sub>3</sub> spectrum is sensitive to changes in the crystal structure, and shows slight differences in Bi 6s<sup>2</sup> states as highlighted by the difference spectra (blue fill) and the inset figure.



after the main absorption line, are structures due to multiple scattering effects.<sup>50</sup> The L<sub>3</sub> edge position in Fig. 4b also shows a 3+ formal charge with small fine structure variations amongst the two samples. The L<sub>3</sub> absorption edge positions for Cs<sub>3</sub>Bi<sub>2</sub>I<sub>9</sub> and BiI<sub>3</sub> are 13 413.9 and 13 413.7 eV respectively. The key spectral changes in the Bi L<sub>3</sub> spectrum are shown in the difference spectra (blue fill) between BiI<sub>3</sub> and Cs<sub>3</sub>Bi<sub>2</sub>I<sub>9</sub> respectively and specifically shown in the pre-edge feature (inset Fig. 4b). Since the lower energy side of the spectrum is expected to come from transitions from occupied 2p to unoccupied anti-bonding 6s states, these differences show the increase in available anti-bonding 6s states for Cs<sub>3</sub>Bi<sub>2</sub>I<sub>9</sub>, representative of a slight change in I p–Bi s hybridization. The difference in the relative intensity and positions of the spectra is attributed to different overlaps between the metal cation and iodine, as an effect of the distances between I and Bi is smaller for Cs<sub>3</sub>Bi<sub>2</sub>I<sub>9</sub> than for BiI<sub>3</sub> (see Table S1 in ESI†). From these two spectra, we suggest that the p character in the conduction band for both samples stays relatively similar with only small differences in the s character as seen from the difference spectra. Since the unoccupied bismuth states of BiI<sub>3</sub> and Cs<sub>3</sub>Bi<sub>2</sub>I<sub>9</sub> show large similarities, it seems appropriate to probe the iodide occupied and unoccupied states to further distinguish the electronic structure.

HERFD-XANES spectra at the Iodine L<sub>1</sub> edge for Cs<sub>3</sub>Bi<sub>2</sub>I<sub>9</sub> and its precursors are shown in Fig. 5 along with the projected electronic density of states (DOS) of Cs<sub>3</sub>Bi<sub>2</sub>I<sub>9</sub> using the LDA functional with SOC. The absorption for the iodine L<sub>1</sub> edge is shown in Fig. 5a. The partial fluorescence yield was detected using the maximum of the L<sub>γ2,3</sub> (5065 eV) emission line. As outlined previously, the advantage of this setup is that the width of the spectral features is no longer limited by the final state 2s core-hole lifetime but by the smaller 4p<sub>3/2</sub> core-hole lifetime. All three samples show distinct spectral features and characters, a consequence of different coordination and displacement of iodine atoms in the unit cell. Although both bismuth compounds show formal Bi<sup>3+</sup>, the sharper white line and higher intensity for BiI<sub>3</sub> could be interpreted as a more localized charge distribution around the I ions in Cs<sub>3</sub>Bi<sub>2</sub>I<sub>9</sub>. This narrowing is likely due to the interlayer nature of the BiI<sub>3</sub> crystal structure. The edge positions (here defined as the zero crossing of the second derivative) for BiI<sub>3</sub>, Cs<sub>3</sub>Bi<sub>2</sub>I<sub>9</sub>, and CsI span an energy

range of 4.2 eV. As the bandgap of the three compounds varies greatly between BiI<sub>3</sub> ( $E_g$ : 1.8 eV), Cs<sub>3</sub>Bi<sub>2</sub>I<sub>9</sub> (2.2 eV), and CsI (6.2 eV), the shift to higher energy for unoccupied iodine states correlates with the observed increase in the bandgap. In contrast to the Bi L<sub>1</sub> and L<sub>3</sub> HERFD-XANES spectra, where the Bi atom occupies a similar coordination in the octahedra, the iodine atoms are displaced in each compound with its own symmetry. These specific crystal structure parameters are directly responsible for the varying features in the spectra. The lack of strong pre-edge features suggests that the counter cation (Cs<sup>+</sup>) is strongly ionic and no mixing exists with I p states at the edge of the conduction band. Feature a in the absorption spectrum for Cs<sub>3</sub>Bi<sub>2</sub>I<sub>9</sub> and BiI<sub>3</sub> is associated with excitations to the first unoccupied p states of iodine, which has covalent character with bismuth s and p states. The subsequent maxima at points (b) and (c) for Cs<sub>3</sub>Bi<sub>2</sub>I<sub>9</sub> and BiI<sub>3</sub> are transitions to hybridized I p and Bi p with the admixture from Cs d states, as seen in the calculated DOS on their right panel for Cs<sub>3</sub>Bi<sub>2</sub>I<sub>9</sub> and BiI<sub>3</sub>. Cs d states contribute mainly in the post-edge region; therefore the conduction band minimum is strictly determined from Bi/I states.

In Fig. 6, RIXS spectra at the I L<sub>1</sub> emission on an energy loss scale are shown. RIXS is highly sensitive to the ligands coordinating to a metal and therefore is an adept tool for probing the ligand coordination environment and valence states.<sup>51</sup> Here, an I 2s (core-electron) is resonantly excited at 5.190 keV for Cs<sub>3</sub>Bi<sub>2</sub>I<sub>9</sub>

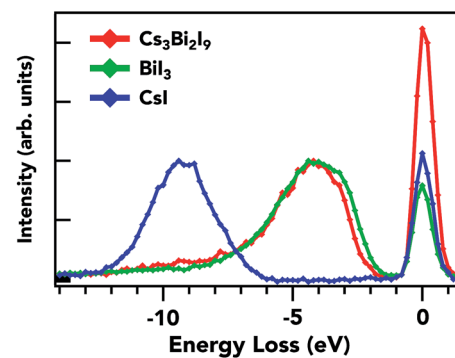


Fig. 6 The RIXS spectra represent contributions of occupied I 5p states in the valence band for the three materials.

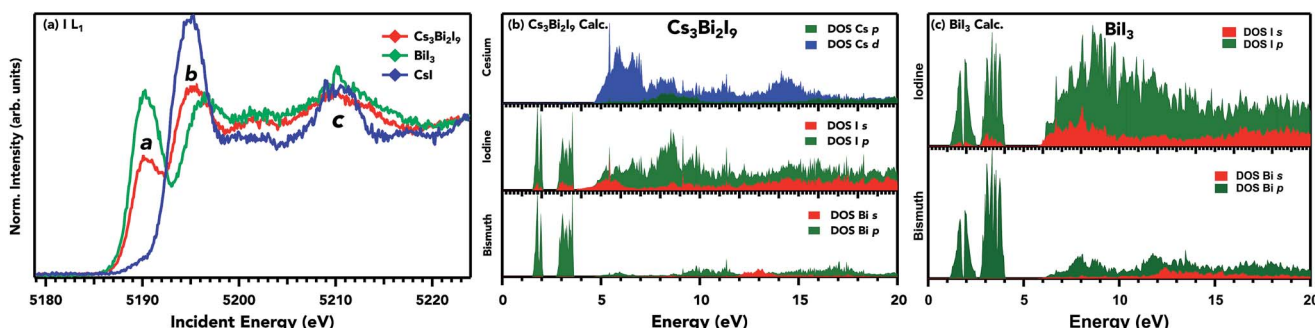


Fig. 5 HERFD-XAS iodine L<sub>1</sub> edge (a) reflects the unoccupied iodine p states in the conduction band and sensitivity to local coordination. The projected DOS in the CB is shown for Cs<sub>3</sub>Bi<sub>2</sub>I<sub>9</sub> (b) and BiI<sub>3</sub> (c).

and  $\text{BiI}_3$  and at 5.195 keV for  $\text{CsI}$ . The spectrometer scans in an energy window that can only be a radiative decay of levels containing  $\text{I}$  5p character, characteristic of the highest occupied orbital. In this case, core-hole effects are negligible due to a high degree of delocalization of  $\text{I}$  5p states. The observed main peak around 4 eV energy loss is from a mix of  $\text{I}$  5p and  $\text{Bi}$  6s, p states. There are no distinguishable features that indicate hybridization with the  $\text{Cs}$  cation, which is expected since its shallow valence levels do not participate in covalent bonding as shown in the next section. Since the excitation energy for the RIXS spectra was set to the first structure in the  $\text{I}$   $\text{L}_1$  XAS spectra, the energy difference between the elastic peak and the onset of the inelastic structures on the energy loss scale correlates with the size of the band gap in these compounds. Therefore, the shift of such an onset to a lower energy loss by 0.4 eV in  $\text{BiI}_3$  as compared with  $\text{Cs}_3\text{Bi}_2\text{I}_9$  indicates a small band gap in the former. This information can provide insight into the changes of  $\text{I}$  p states, and how they ultimately affect the band gap. These results also suggest that the  $\text{Cs}$  cation has no direct effect on varying the band gap of  $\text{Cs}_3\text{Bi}_2\text{I}_9$ , as was shown by DFT calculations recently.<sup>52</sup>

The experimental valence band for the three samples on  $\text{mTiO}_2$  and valence DFT calculations for  $\text{Cs}_3\text{Bi}_2\text{I}_9$  and  $\text{BiI}_3$  are shown in Fig. 7. The overall spectral shape of  $\text{Cs}_3\text{Bi}_2\text{I}_9$  has a structure that follows the characteristics of that of the precursors, with modification in the valence band edge position in between the low bandgap  $\text{BiI}_3$  and high bandgap  $\text{CsI}$ . The high photon energy of 4000 eV provides a relatively bulk sensitive probe. The ionization cross-sections for  $\text{Bi}$  5p and 6s states are nearly the same as that of  $\text{I}$  5p at 4000 eV. The doublet peak near  $\sim$ 12 eV corresponds to  $\text{Cs}$  5p orbitals, states that do not participate in bonding. The calculated partial and total density of states along with experimental spectra in the valence band are presented in Fig. 7b. The spectra are dominated by  $\text{I}$  5p states extending from the valence band onset to about 6–8 eV in binding energy. The data are in general agreement with the calculated spectra presented here; however small discrepancies are common when comparing experimental photoemission to that of DFT calculations. The plot shows the calculated

contributions of  $\text{I}$  5p and  $\text{Bi}$  6s/5p states, along with the total calculated DOS and experimental photoemission data. The DFT results are in close agreement with other DFT calculations using the Generalized Gradient Approximation (GGA) and the projector-augmented wave (PAW) formalism.<sup>18,19</sup> The  $\text{Cs}$  contribution to the VB is near 10 eV, and therefore does not participate in bonding with the frontier states of bismuth and iodine.  $\text{I}$  p states hybridize to a small degree with  $\text{Bi}$  lone pair s states towards the edge of the valence band. The mixing of ligand and lone pair states is crucial in producing asymmetric electron density in the  $\text{Bi}$  ion.<sup>53</sup> This mixing produces filled bonding and anti-bonding states that give its ‘defect-tolerant’ properties within the valence band.

### 3.3 Valence band structure and interfacial energetics

The determination of experimental band positions is a critical step in the evaluation of the material electronic properties and their role in photovoltaic design. The relative position of the three materials in relation to the conduction band minimum (CBM) of titania is imperative for electron transfer and voltage loss in the device. An approximation of the valence band maximum (VBM) can be interpreted by taking the linear extrapolation on the low binding energy end of the VB HAXPES spectrum, in accordance with the location of the Fermi level set by the gold  $\text{Au}$   $4\text{f}_{7/2}$  spectra as shown in Fig. 8. The band gap is derived from Tauc plots (ESI: Fig. S2†) and is used to determine the CB minimum (CBM). The energy difference of the valence band edges between  $\text{TiO}_2$  and the halide compounds is  $-1.73$  eV,  $-1.93$  eV, and  $-1.05$  for  $\text{Cs}_3\text{Bi}_2\text{I}_9$ ,  $\text{BiI}_3$ , and  $\text{CsI}$  respectively. From this representation, the band edges of  $\text{Cs}_3\text{Bi}_2\text{I}_9$  and  $\text{BiI}_3$  are well matched for the electron transport material  $\text{mTiO}_2$  and favorable for electron transfer without significant loss. The relevant data on the band positions of the conduction band minimum (CBM) and valence band maximum (VBM) provide a means to determine the material requirements for appropriate interfacial layers in solar cells. This shows the efficacy of using HAXPES in order to determine relative band-offsets in light harvesting materials.

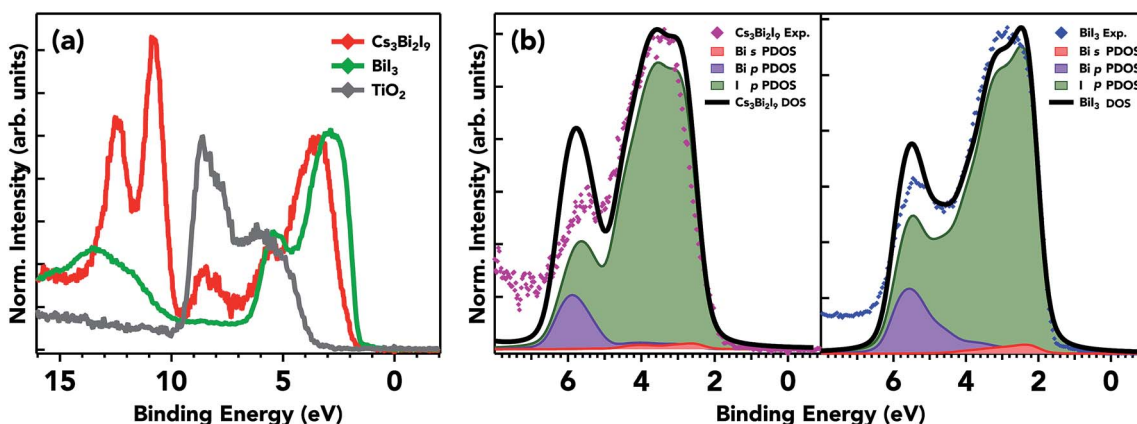


Fig. 7 Valence band spectra for the three samples at 4000 eV (a) and calculated VB pDOS for  $\text{Cs}_3\text{Bi}_2\text{I}_9$  and  $\text{BiI}_3$  (b). DFT calculations showing the partial and total density of states along with experimental spectra in the valence band. The principal differences in the two samples are the positions and weight of the  $\text{Bi}$  s states in the VB. The  $\text{I}$  p character is almost the same in terms of spectral weight and features.



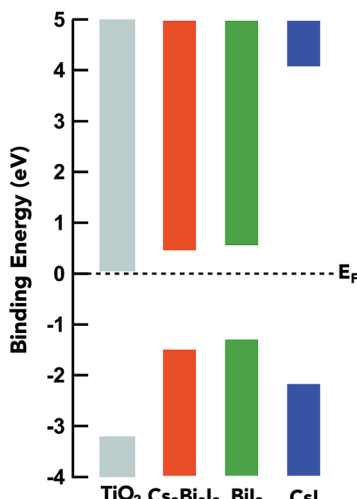


Fig. 8 The energy level alignment between m $\text{TiO}_2$  and the samples measured using HAXPES measurements. Optical band gaps for the samples are estimated from UV-Vis absorption spectra.

## 4 Conclusions

In summary, we used several X-ray spectroscopic techniques along with support from DFT calculations to investigate the electronic structure and band energetics of  $\text{Cs}_3\text{Bi}_2\text{I}_9$ ,  $\text{BiI}_3$ , and  $\text{CsI}$ . HERFD-XAS at the Bi  $\text{L}_1$  and  $\text{L}_3$  edges shows very similar local coordination for Bi atoms in both  $\text{Cs}_3\text{Bi}_2\text{I}_9$  and  $\text{BiI}_3$ , with a modest increase in available Bi s in the CB for  $\text{Cs}_3\text{Bi}_2\text{I}_9$ . The complimentary RIXS data also show a similar VB profile of the highest occupied p states, with changes only in the position of I 5p occupied states. HAXPES data show a similar spectral profile towards the band edge, and calculations revealed very similar mixing of I p states and Bi s and Bi p states. The primary significance was the position of the VBM, which is used to construct the interfacial profile against a m $\text{TiO}_2$  interface to show a favorable electronic transport in optoelectronic applications. These findings demonstrate the utility of hard X-ray spectroscopy in identifying detailed electronic structures and their use in solar harvesting devices.

## Conflicts of interest

There are no conflicts to declare.

## Acknowledgements

We acknowledge financial support from the Swedish Research Council (2014-6019, 2016-4524), the Swedish Energy Agency (P43549-1), the Swedish Foundation for Strategic Research (15-0130), the Wallenberg Foundation (2012.0031), and the StandUP for Energy. HZB and ESRF are acknowledged for the allocation of synchrotron radiation beamtime. The computations were performed on resources provided by the Swedish National Infrastructure for Computing (SNIC) at the Swedish National Supercomputer Center (NSC).

## Notes and references

- M. M. Lee, J. Teuscher, T. Miyasaka, T. N. Murakami and H. J. Snaith, *Science*, 2012, **338**, 643–647.
- H.-S. Kim, C.-R. Lee, J.-H. Im, K.-B. Lee, T. Moehl, A. Marchioro, S.-J. Moon, R. Humphry-Baker, J.-H. Yum, J. E. Moser, M. Grätzel and N.-G. Park, *Sci. Rep.*, 2012, **2**, 591.
- J. Luo, J.-H. Im, M. T. Mayer, M. Schreier, M. K. Nazeeruddin, N.-G. Park, S. D. Tilley, H. J. Fan and M. Grätzel, *Science*, 2014, **345**, 1593–1596.
- Z.-K. Tan, R. S. Moghaddam, M. L. Lai, P. Docampo, R. Higler, F. Deschler, M. Price, A. Sadhanala, L. M. Pazos, D. Credgington, F. Hanusch, T. Bein, H. J. Snaith and R. H. Friend, *Nat. Nanotechnol.*, 2014, **9**, 1–6.
- G. Xing, N. Mathews, S. S. Lim, N. Yantara, X. Liu, D. Sabba, M. Grätzel, S. Mhaisalkar and T. C. Sum, *Nat. Mater.*, 2014, **13**, 476–480.
- O. A. Jaramillo-Quintero, R. S. Sánchez, M. Rincón and I. Mora-Sero, *J. Phys. Chem. Lett.*, 2015, **6**, 1883–1890.
- F. Zhang, H. Zhong, C. Chen, X.-g. Wu and X. Hu, *ACS Nano*, 2015, **9**, 4533–4542.
- X. Y. Chin, D. Cortecchia, J. Yin, A. Bruno and C. Soci, *Nat. Commun.*, 2015, **6**, 7383.
- N. J. Jeon, J. H. Noh, Y. C. Kim, W. S. Yang, S. Ryu and S. I. Seok, *Nat. Mater.*, 2014, **13**, 897–903.
- T.-b. Song, Q. Chen, H.-P. Zhou, C. Jiang, H.-H. Wang, Y. Yang, Y. Liu and J. You, *J. Mater. Chem. A*, 2015, **3**, 9032–9050.
- P. Fan, D. Gu, G.-X. Liang, J.-T. Luo, J.-L. Chen, Z.-H. Zheng and D.-P. Zhang, *Sci. Rep.*, 2016, **6**, 29910.
- L. K. Ono, M. R. Leyden, S. Wang and Y. Qi, *J. Mater. Chem. A*, 2016, **4**, 6693–6713.
- S. M. Jain, B. Philippe, E. M. J. Johansson, B.-w. Park, H. Rensmo, T. Edvinsson and G. Boschloo, *J. Mater. Chem. A*, 2016, **4**, 2630–2642.
- A. Babayigit, D. Duy Thanh, A. Ethirajan, J. Manca, M. Muller, H.-G. Boyen and B. Conings, *Sci. Rep.*, 2016, **6**, 18721.
- T. Leijtens, G. E. Eperon, N. K. Noel, S. N. Habisreutinger, A. Petrozza and H. J. Snaith, *Adv. Energy Mater.*, 2015, **5**, 1500963.
- B. Philippe, B. W. Park, R. Lindblad, J. Oscarsson, S. Ahmadi, E. M. J. Johansson and H. Rensmo, *Chem. Mater.*, 2015, **27**, 1720–1731.
- B.-W. Park, B. Philippe, X. Zhang, H. Rensmo, G. Boschloo and E. M. J. Johansson, *Adv. Mater.*, 2015, **27**, 6806–6813.
- A. J. Lehner, D. H. Fabini, H. A. Evans, C. A. Hébert, S. R. Smock, J. Hu, H. Wang, J. W. Zwanziger, M. L. Chabiny and R. Seshadri, *Chem. Mater.*, 2015, **27**, 7137–7148.
- M. Pazoki, M. B. Johansson, H. Zhu, P. Broqvist, T. Edvinsson, G. Boschloo and E. M. J. Johansson, *J. Phys. Chem. C*, 2016, **120**, 29039–29046.
- A. T. Lintereur, W. Qiu, J. C. Nino and J. Baciak, *Nucl. Instrum. Methods Phys. Res., Sect. A*, 2011, **652**, 166–169.



21 P. M. Johns, J. E. Baciak and J. C. Nino, *Appl. Phys. Lett.*, 2016, **109**, 092105.

22 R. E. Brandt, R. C. Kurchin, R. L. Z. Hoye, J. R. Poindexter, M. W. B. Wilson, S. Sulekar, F. Lenahan, P. X. T. Yen, V. Stevanovic, J. C. Nino, M. G. Bawendi and T. Buonassisi, *J. Phys. Chem. Lett.*, 2015, **6**, 4297–4302.

23 A. Farzaneh, M. R. Abdi, K. R. E. Saraee, M. Mostajaboddavati and A. Quaranta, *Opt. Mater.*, 2016, **55**, 22–26.

24 G. Papavassiliou, I. Koutselas, A. Terzis and M.-H. Whangbo, *Solid State Commun.*, 1994, **91**, 695–698.

25 A. Walsh, D. J. Payne, R. G. Egddell and G. W. Watson, *Chem. Soc. Rev.*, 2011, **40**, 4455–4463.

26 R. E. Brandt, V. Stevanović, D. S. Ginley and T. Buonassisi, *MRS Commun.*, 2015, **5**, 1–11.

27 L. Y. Huang and W. R. L. Lambrecht, *Phys. Rev. B: Condens. Matter Mater. Phys.*, 2013, **88**, 1–12.

28 A. M. Ganose, K. T. Butler, A. Walsh and D. O. Scanlon, *J. Mater. Chem. A*, 2016, **4**, 2060–2068.

29 B. Chabot and E. Parthe, *Acta Crystallogr., Sect. B: Struct. Crystallogr. Cryst. Chem.*, 1978, **34**, 645–648.

30 A. Jorio, R. Currat, D. Myles, G. McIntyre, I. Aleksandrova, J. Kiat and P. Saint-Grégoire, *Phys. Rev. B: Condens. Matter Mater. Phys.*, 2000, **61**, 3857–3862.

31 R. T. Poole, J. G. Jenkin, J. Liesegang and R. C. G. Leckey, *Phys. Rev. B: Solid State*, 1975, **11**, 5179–5189.

32 B. Philippe, M. Saliba, J. P. Correa-Baena, U. B. Cappel, S. H. Turren-Cruz, M. Grätzel, A. Hagfeldt and H. Rensmo, *Chem. Mater.*, 2017, **29**, 3589–3596.

33 W. S. Drisdell, L. Leppert, C. M. Sutter-Fella, Y. Liang, Y. Li, Q. P. Ngo, L. F. Wan, S. Gul, T. Kroll, D. Sokaras, A. Javey, J. Yano, J. B. Neaton, F. M. Toma, D. Prendergast and I. D. Sharp, *ACS Energy Lett.*, 2017, **2**, 1183–1189.

34 M. Gorgoi, S. Svensson, F. Schäfers, G. Öhrwall, M. Mertin, P. Bressler, O. Karis, H. Siegbahn, A. Sandell, H. Rensmo, W. Doherty, C. Jung, W. Braun and W. Eberhardt, *Nucl. Instrum. Methods Phys. Res., Sect. A*, 2009, **601**, 48–53.

35 J. H. Scofield, UCRL-51326: Theoretical Photoionization Cross Sections from 1 to 1500 keV, University of California-Livermore, 1973, vol. 257, p. 374.

36 C. Gauthier, V. A. Solé, R. Signorato, J. Goulon and E. Moguiline, *J. Synchrotron Radiat.*, 1999, **6**, 164–166.

37 K. O. Kvashnina and A. C. Scheinost, *J. Synchrotron Radiat.*, 2016, **23**, 836–841.

38 A. J. Atkins, C. R. Jacob and M. Bauer, *Chem.-Eur. J.*, 2012, **18**, 7021–7025.

39 J. M. Wills, O. Eriksson, M. Alouani and D. L. Price, *Electronic Structure and Physical Properties of Solids: the Uses of the LMTO Method*, Springer-Verlag Berlin Heidelberg, 2000.

40 O. Lindqvist, G. Johansson, F. Sandberg and T. Norin, *Acta Chem. Scand.*, 1968, **22**, 2943–2952.

41 J. Trotter and T. Zobel, *Z. Kristallogr. Krist.*, 1966, **123**, 67–72.

42 C. Ortiz, O. Eriksson and M. Klintenberg, *Comput. Mater. Sci.*, 2009, **44**, 1042–1049.

43 W. Zhang, S. Pathak, N. Sakai, T. Stergiopoulos, P. K. Nayak, N. K. Noel, A. A. Haghaghirad, V. M. Burlakov, D. W. DeQuilettes, A. Sadhanala, W. Li, L. Wang, D. S. Ginger, R. H. Friend and H. J. Snaith, *Nat. Commun.*, 2015, **6**, 10030.

44 W. Xu, L. Liu, L. Yang, P. Shen, B. Sun and J. A. McLeod, *Nano Lett.*, 2016, **16**, 4720–4725.

45 G. Sadoughi, D. E. Starr, E. Handick, S. D. Stranks, M. Gorgoi, R. G. Wilks, M. Bär and H. J. Snaith, *ACS Appl. Mater. Interfaces*, 2015, **7**, 13440–13444.

46 B. Philippe, B. W. Park, R. Lindblad, J. Oscarsson, S. Ahmadi, E. M. J. Johansson and H. Rensmo, *Chem. Mater.*, 2015, **27**, 1720–1731.

47 M. Trzhaskovskaya, V. Nefedov and V. Yarzhemsky, *At. Data Nucl. Data Tables*, 2001, **77**, 97–159.

48 M. Trzhaskovskaya, V. Nefedov and V. Yarzhemsky, *At. Data Nucl. Data Tables*, 2002, **82**, 257–311.

49 M. Bauer, *Phys. Chem. Chem. Phys.*, 2014, **16**, 13827–13837.

50 J. J. Rehr, *Rev. Mod. Phys.*, 2000, **72**, 621–654.

51 E. R. Hall, C. J. Pollock, J. Bendix, T. J. Collins, P. Glatzel and S. Debeer, *J. Am. Chem. Soc.*, 2014, **136**, 10076–10084.

52 X. Huang, S. Huang, P. Biswas and R. Mishra, *J. Phys. Chem. C*, 2016, **120**, 28924–28932.

53 A. Walsh, G. W. Watson, D. J. Payne, R. G. Edgell, J. Guo, P.-A. Glans, T. Learmonth and K. E. Smith, *Phys. Rev. B: Condens. Matter Mater. Phys.*, 2006, **73**, 235104.

